nature water

Article

https://doi.org/10.1038/s44221-023-00150-0

Scalable and efficient solar-driven atmospheric water harvesting enabled by bidirectionally aligned and hierarchically structured nanocomposites

Received: 28 February 2023

Accepted: 2 October 2023

Published online: 30 October 2023

Check for updates

Tingxian Li[1,2,4] ✉, Taisen Yan[2,4], Pengfei Wang[2,4], Jiaxing Xu[2], Xiangyan Huo[2], Zhaoyuan Bai[2], Wen Shi[3], Guihua Yu[3] ✉ & Ruzhu Wang[1,2] ✉

Extracting water from air is a promising route to address the global challenge of water scarcity. Sorption-based atmospheric water harvesting (SAWH) has the capability of capturing water from air anytime and anywhere. However, low water production is a long-standing challenge for realizing efficient SAWH. Here we report a facile strategy to synthesize bidirectionally aligned and hierarchically structured nanocomposite (BHNC) for scalable and efficient SAWH. Benefiting from the synergetic effects of ordered hierarchical structures for accelerating vertically oriented moisture convection and radially oriented intrapore diffusion, the BHNC exhibits ultrahigh water uptake of 6.61 kg_{water} $kg_{sorbent}^{-1}$ and ultrafast water sorption kinetics, superior to the state-of-the-art sorbents. We further engineer a scalable and efficient solar-driven SAWH prototype by assembling BHNC arrays, demonstrating rapid-cycling and high-yielding water production up to 2,820 ml_{water} $kg_{sorbent}^{-1}$ day^{-1}. This work provides new insights to bridge the gap between materials and devices for scalable, energy efficient and all-weather water harvesting from air powered by solar energy.

Water scarcity is one of the most serious global challenges for sustainable development[1]. Atmospheric moisture, approximately six times more than the water in all rivers on Earth, is a potential water source[2]. Benefiting from the interaction between moisture and water-affinity sorbents, sorption-based atmospheric water harvesting (SAWH) shows distinct adaptability and flexibility to capture water from air anytime and anywhere. Considering the sunlight and ubiquitous moisture, solar-driven SAWH is considered an eco-friendly technology for producing water[3–7].

Various high-performance sorbents, such as metal–organic frameworks[8–11], covalent organic frameworks[12–15] and salt-based composites[16–20], provide substantial material candidates for SAWH. Salt-based composites, defined as confining hygroscopic salts in porous matrices[21,22], especially have attracted extensive attention due to low costs, high water uptake and superior climate adaptability. However, slow sorption/desorption kinetics of packed sorbents are long-standing bottlenecks for realizing efficient SAWH due to the poor heat

[1]Research Center of Solar Power and Refrigeration, Ministry of Education of China, Shanghai, China. [2]Institute of Refrigeration and Cryogenics, School of Mechanical Engineering, Shanghai Jiao Tong University, Shanghai, China. [3]Materials Science and Engineering Program and Department of Mechanical Engineering, The University of Texas at Austin, Austin, TX, USA. [4]These authors contributed equally: Tingxian Li, Taisen Yan, Pengfei Wang.
✉e-mail: Litx@sjtu.edu.cn; Ghyu@austin.utexas.edu; Rzwang@sjtu.edu.cn

transfer and mass transport when massive sorbent particles are packed in SAWH devices[23]. The slow sorption/desorption kinetics prolong the equilibrium time, resulting in low water production of SAWH devices. Therefore, it is highly needed to accelerate water sorption/desorption kinetics by uncovering the essence of the structure–performance relationship of packed sorbents[24,25].

Substantial efforts have been paid to develop new sorbents in the past decade[26], but little attention has been focused on the thermal design of SAWH devices. Although advanced sorbents exhibit superior sorption performance, the reported SAWH devices show relatively low water productivity due to the poor heat transfer and mass transport of packed sorbents, hindering their practical applications. It is urgent to make comprehensive innovations on SAWH systems at both material and device levels[27,28]. The key issue for high-performance SAWH is to search for superior SAWH sorbents with high water uptake capacity, scalable SAWH devices with excellent heat and mass transfer and energy-saving SAWH systems with high energy efficiency.

Here we reveal the essence of the structure–performance relationship of packed sorbents and discuss the influence of different structures on water sorption/desorption kinetics. Inspired by the theoretical analysis, we report a new strategy to fabricate bidirectionally aligned and hierarchically structured nanocomposites (BHNC) for atmospheric water harvesting. Benefiting from the synergetic effects of vertically oriented moisture convection and radially oriented intrapore diffusion, the resultant BHNC exhibits ultrahigh water uptake of 6.61 kg_{water} $kg_{sorbent}^{-1}$ and ultrafast water sorption kinetics.

Moreover, we engineer a scalable and efficient solar-driven SAWH prototype and propose an energy-saving strategy to realize energy efficient SWAH with synergistic effects: lowering the cooling temperature of water condensation and decreasing the energy consumption for water desorption simultaneously. The well-designed solar-driven SAWH device achieves high-yielding water production of up to 2,820 ml_{water} $kg_{sorbent}^{-1}$ day^{-1}. Our work provides new insights to bridge the gap between SAWH materials and devices for scalable, energy efficient and high-yielding atmospheric water harvesting.

Results

Conceptual structure with superior water transport kinetics

Water vapour transport inside packed sorbents directly influences the kinetics of water capture and release (Fig. 1a). Generally, the sorption kinetics are determined by multi-step water transport processes, undergoing surface resistance, diffusion resistance and reaction resistance[29–32] (Fig. 1b). Serious deterioration of sorption/desorption kinetics is a common bottleneck for all kinds of large-scale packed sorbents, which is mainly ascribed to the increased diffusion resistances of water vapour transport. To address the common challenge, we systematically discuss the variation of transport resistances during morphological evolution of packed structures (Fig. 1c).

Increasing the porosity is a feasible way to lower the diffusion resistance, while high porosity will inevitably cause the reduction of packed sorbents in devices. There remains a trade-off between sorption/desorption kinetics and water uptake when optimizing the porosity of packed sorbents. Therefore, the key research point for lowering diffusion resistance is to regulate the diffusion depth and tortuosity factor.

The unordered structure of packed sorbents is the common arrangement for SAWH devices[5,7] but suffers from high diffusion resistance due to long diffusion depth and high tortuosity factor. Some modified unidirectional structures are proposed to decrease diffusion resistance by reducing diffusion depth or internal tortuosity, for instance, vertically aligned nanocomposites with low tortuosity[32] and honeycomb-structured hygroscopic polymer with reduced diffusion depth[33]. Considering the fact that diffusion resistance is mainly determined by diffusion depth and tortuosity factor, rational design of new packed structures with optimized diffusion depth and tortuosity factor is expected to overcome the common bottleneck of low sorption/desorption kinetics.

We develop theoretical models to analyse the sorption/desorption kinetics of different packed structures (Extended Data Fig. 1 and Supplementary Note 1), and these models are validated by experimental results[32] (Supplementary Fig. 1 and Supplementary Table 1). The simulation results indicate diffusion resistance plays a dominant role in the overall resistance during water transport (Supplementary Figs. 2–4). The overall mass transport resistance ($R_{m,total}$) can be decreased significantly by improving the orderliness of packed structures (Fig. 1d). For instance, the unidirectional structure has low mass transport resistance, only 1/10 of unordered structure and the mass transport resistance can be further lowered by 60% when transformed to bidirectional structure (Fig. 1d). Moreover, the overall heat transfer resistance ($R_{T,total}$) can also be decreased dramatically during the morphological evolutions from unordered structure to unidirectional or bidirectional structure (Fig. 1e). Contributed by the low resistance, the bidirectional and unidirectional structures exhibit faster sorption kinetics and higher water uptake than the unordered structure (Supplementary Fig. 5).

We further verify the influence of diffusion depth on water uptake by a single variable method (Supplementary Fig. 6). The water uptake becomes very low with increased diffusion depth for the unordered structure, indicating the deterioration of water transport. Interestingly, the packed thickness has negligible influence on the bidirectional structure due to the diffusion depth being changed from the packed thickness to half of the interval between the adjacent honeycomb-like channels. Therefore, the short diffusion depth and low tortuosity factor endow superior water transport kinetics of bidirectional structure.

Fabrication and characterization of BHNC

Bidirectionally structured sorbents show great potential to realize efficient and high-yielding SAWH according to the above analysis. We propose a new strategy for synthesizing scalable BHNC blocks with ordered hierarchical structures by designing bidirectionally aligned porous graphene hydrogel matrix (BPGHM) with hygroscopic lithium chloride (LiCl) coating. The synthesis procedure of BHNC mainly includes bidirectional freezing assembly, freeze drying, cross linking and salt loading (Fig. 2a and Methods).

Unlike conventional unidirectional freeze-casting methods[34], a special copper template with arrayed copper pillars (Supplementary Fig. 7) is carefully designed to prepare BPGHM with ordered hierarchical structures. Liquid nitrogen-induced bidirectional ice crystal grows in the graphene oxide and sodium alginate (GO-SA) solution subjected to two temperature gradients: vertical temperature gradient (ΔT_V) and radial temperature gradient (ΔT_R). The infrared images verified the additional radial temperature gradient of the bidirectional freeze-casting method (Extended Data Fig. 2). Benefiting from copper pillars and bidirectional ice crystal growth, a bidirectional hierarchical structure with vertically oriented and radially oriented microchannels is formed after removing ice crystals (Extended Data Fig. 3).

Scanning electron micrograph (SEM) image from the top view (Fig. 2b) shows that millimetre-scale cylindrical through holes uniformly distribute in BPGHM, providing accessible convective paths and short diffusion depth during water transport. The enlarged images show micrometre-scale pores are radially along with the arrayed through holes. The SEM images of the cross-sectional view (Fig. 2c) show that micrometre-scale channels are vertically distributed from the bottom to the top surfaces of BPGHM, with plentiful micrometre-sized pores. The BPGHM is further strengthened by calcium ions cross-linking reaction (Extended Data Fig. 3g–i) and thermal reduction (Supplementary Fig. 8), where the vertically and radially hierarchical structures are well retained. LiCl is selected as the hygroscopic salt to be confined into the prepared BPGHM to fabricate scalable BHNC block due to its superior water sorption capacity[16]. The enlarged SEM images

https://doi.org/10.1038/s44221-023-00150-0

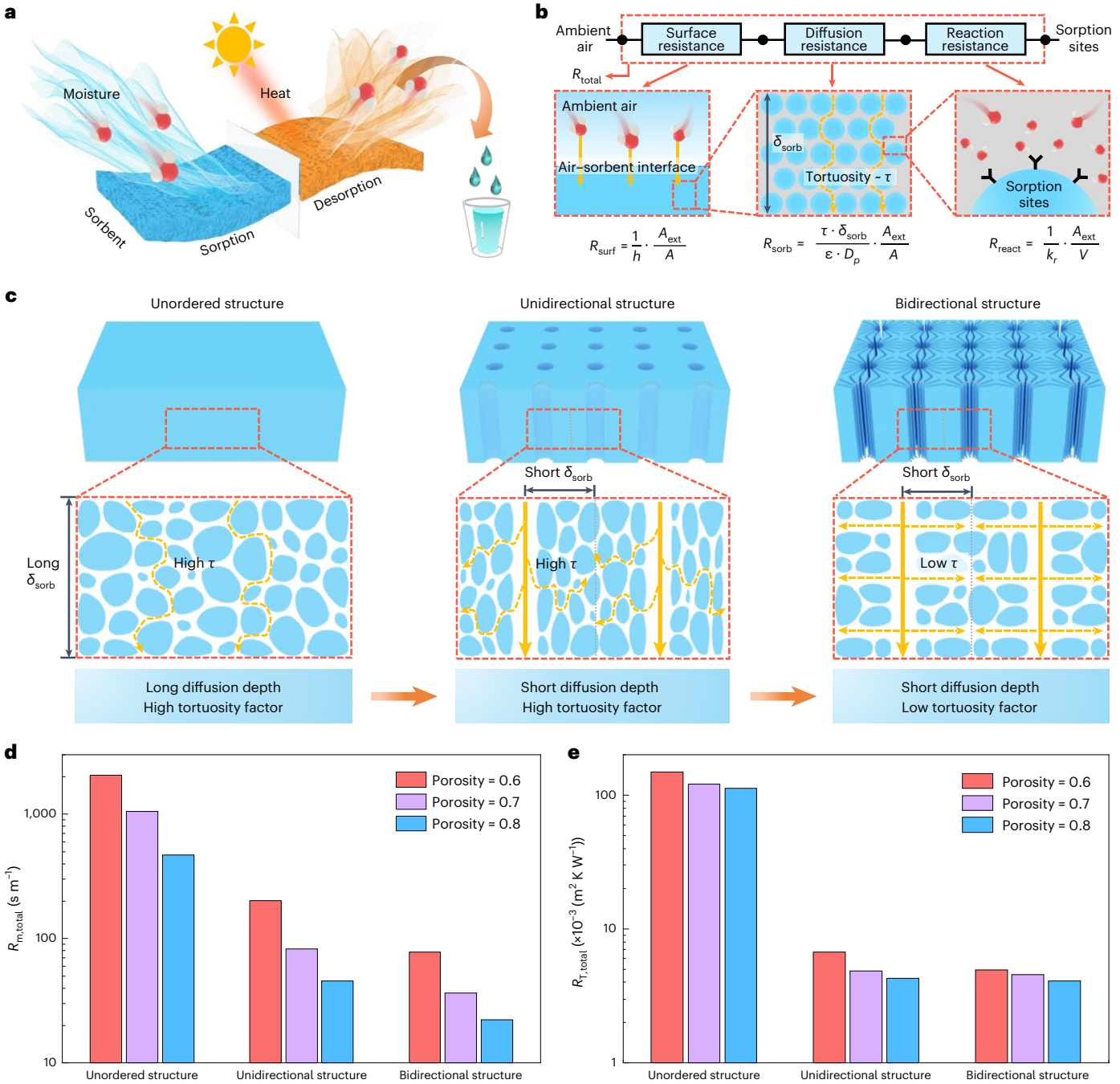

Fig. 1 | Conceptual design of packed sorbents with superior water transport kinetics. a, Schematic of water sorption from air and water desorption from sorbent during water harvesting. **b**, Schematic of multi-step moisture transport during water sorption process. Water molecules transport from the ambient air to the external surface of sorbents by undergoing surface resistance (R_{surf}), which can be tuned by the external airflow rate. Subsequently, the water molecules further diffuse along the connected intrapores by overcoming diffusion resistance (R_{sorb}), which is mainly affected by the tortuosity factor (τ), the diffusion depth (δ_{sorb}) and packed porosity (ε). Finally, the water molecules are captured by the sorption sites of sorbents, mainly determined by the intrinsic reaction resistance (R_{react}). **c**, Morphological evolution from unordered structures to ordered structures of packed sorbents with enhanced heat transfer and mass transport. **d**, Numerical results of the total mass transport resistances of different packed structures. **e**, Numerical results of the total heat transfer resistances of different packed structures.

(Fig. 2d) and elemental mapping with energy dispersive X-ray spectroscopy (EDX) (Supplementary Fig. 9) show that submicrometre-size LiCl crystals are evenly coated on the surfaces of BPGHM, preventing the agglomeration of salt particles.

The comparison between the pore distributions of BPGHM and BHNC block (Fig. 2e) indicates these 20–100 μm pores are mainly occupied by LiCl crystals, and some enlarged pores with sizes of 100–1,000 μm remain as water transport channels. The X-ray photoelectron spectroscopy (XPS) patterns (Supplementary Fig. 10) show that BPGHM has plentiful oxygen-containing function groups and the ratio of C/O is around 3.0, enabling hydrophilic characters with a contact angle of 59° and the contact angle of BHNC can be lowered to 6° (Supplementary Fig. 11).

Compared to the reported freeze-casting methods[35–38] and salt-based composites[16–20], our strategy has distinct capability of fabricating scalable, bidirectionally aligned and hierarchically structured porous matrices and

https://doi.org/10.1038/s44221-023-00150-0

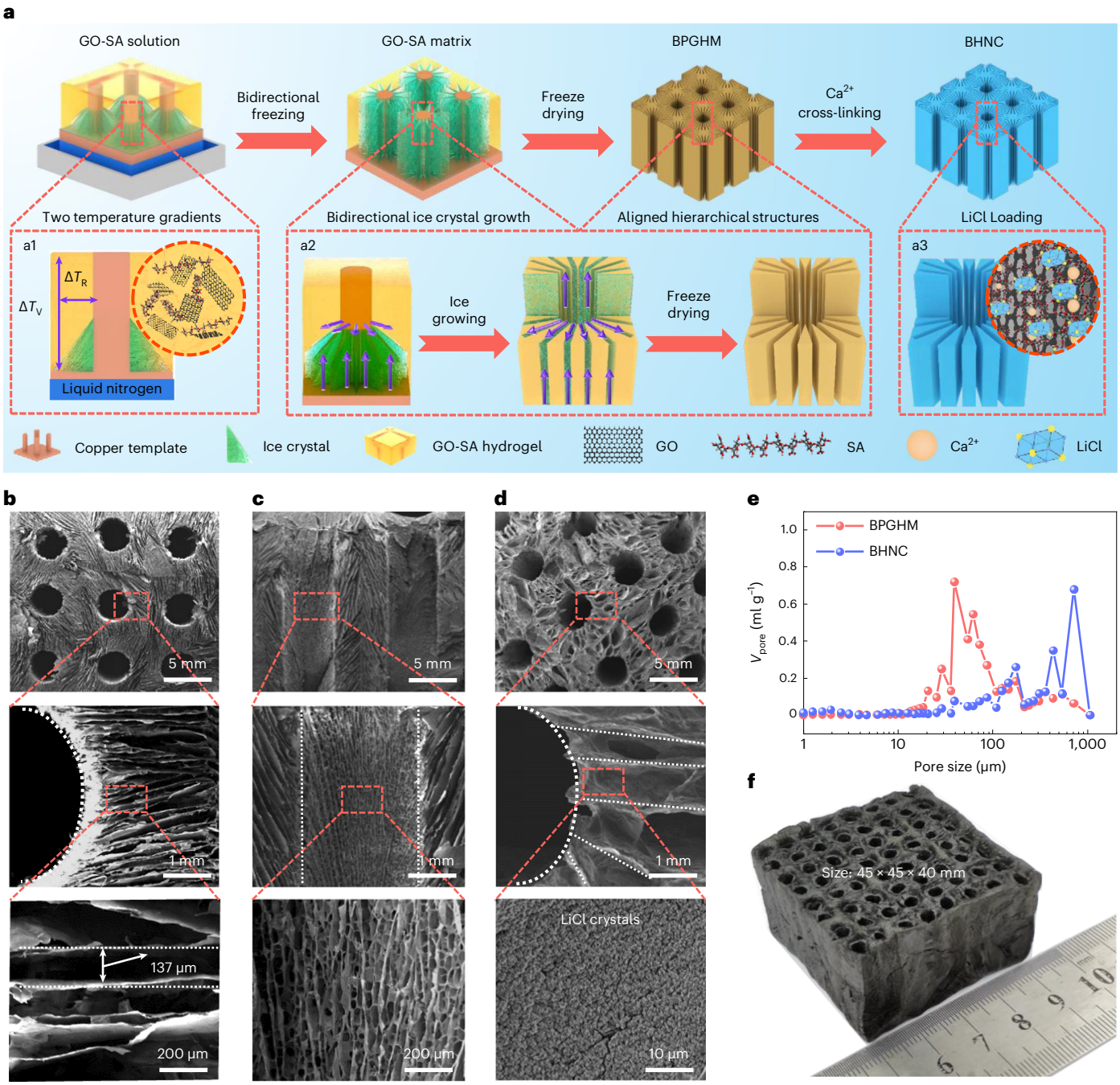

Fig. 2 | Synthesis and characterization of BHNC. a, Synthesis procedures of bidirectionally aligned and hierarchically structured nanocomposites mainly include bidirectional freezing assembly, freeze drying, cross linking and salt loading. The vertically oriented and radially oriented hierarchical structures are formed enabled by two temperature gradients: vertical temperature gradient (ΔT_V) for driving ice growth from the bottom copper base to the top of the graphene oxide and sodium alginate (GO-SA) solution and radial temperature gradient (ΔT_R) for driving ice growth from the copper pillars to the circumferential GO-SA solution. **b**, SEM images of BPGHM from the top view. **c**, SEM images of BPGHM from a cross-sectional view. **d**, SEM images of BHNC after Ca^{2+} cross linking and LiCl loading, showing nano-size LiCl crystals are evenly distributed on the surface of BPGHM as salt coating. **e**, Pore size distributions of BPGHM and BHNC. **f**, Digital photograph of scalable BHNC block with the size of 45 mm (L) × 45 mm (W) × 40 mm (H).

salt-based composites with self-assembly ordered structures (Fig. 2f). Moreover, the shape and size of vertically and radially oriented channels in BHNC block can be easily tuned by changing the length and distance of arrayed metallic pillars of moulds. This strategy can be extended to a large variety of sorbents, even not limited to the field of SAWH.

Water sorption performance of BHNC

The BHNC exhibits superior water uptake capacity benefiting from multi-step water sorption processes (Fig. 3a), solid–gas chemisorption at low relative humidity (RH), liquid–gas deliquescence at moderate RH and liquid–gas absorption at high RH. The multi-step water sorption is confirmed by the comparison of X-ray diffraction (XRD) patterns between BPGHM (Supplementary Fig. 12) and BHNC (Supplementary Fig. 13). We also analysed the equilibrium water uptake during the chemisorption, deliquescence and absorption processes (Supplementary Note 2.1), providing a guideline for designing high-performance salt-based composites.

This BHNC exhibits high water uptake up to 0.9 $g_{water}\ g_{sorbent}^{-1}$ even at as low as 15% RH, and the water uptake can be further increased to

https://doi.org/10.1038/s44221-023-00150-0

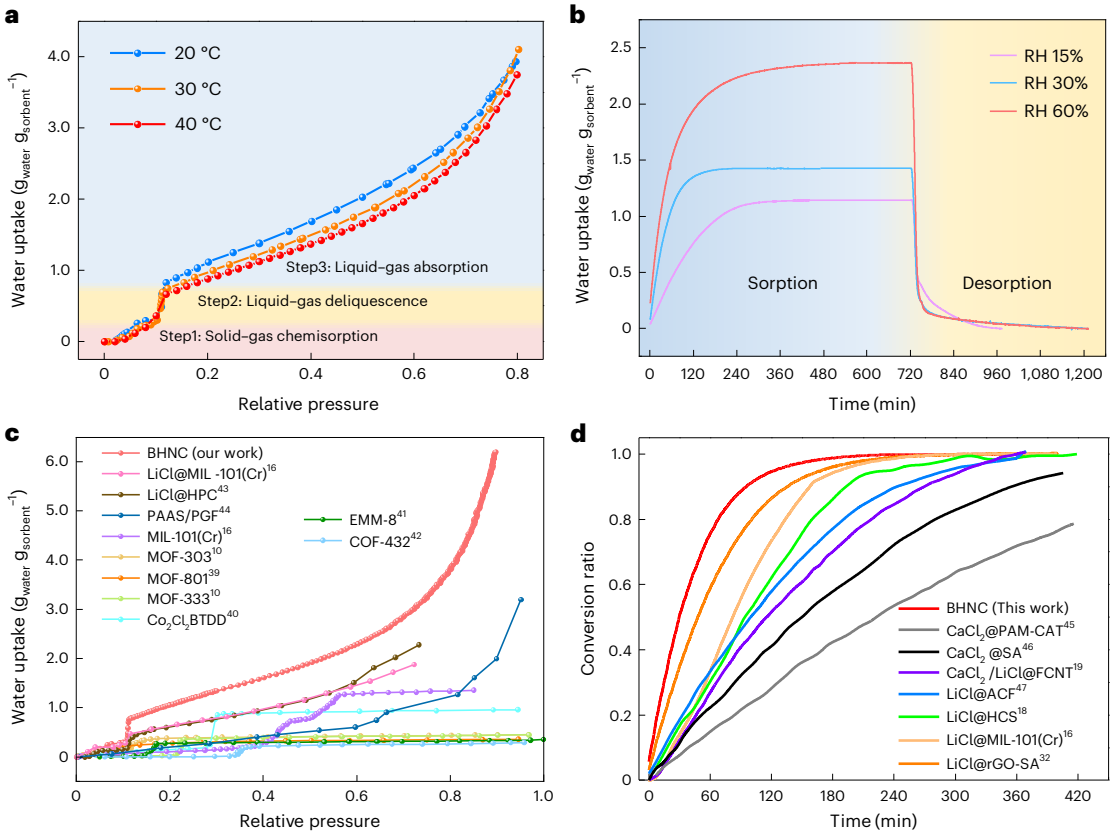

Fig. 3 | Water sorption capacity of BHNC. a, Multi-step water sorption processes of BHNC at different temperatures, including solid–gas chemisorption from LiCl to LiCl·H_2O at low RH, liquid–gas deliquescence from LiCl·H_2O to saturated LiCl solution at moderate RH and liquid–gas absorption from saturated LiCl solution to dilute LiCl solution at high RH. **b**, Thermogravimetric analysis and differential scanning calorimetry (TG-DSC) curves of BHNC under 30 °C with RH range from 15% to 60% for water sorption (15%, 30%, 60%) and 90 °C at 4,200 Pa for water desorption. **c**, Comparison of water uptake between our BHNC and reported state-of-the-art sorbents for SAWH[10,16,39–44]. **d**, Comparison of water sorption kinetics between our BHNC and reported state-of-the-art salt-based composites[16,18,19,32,45–47] in arid climates under 20–40% RH; the conversion ratio can be calculated as q/q_{max} (details in Supplementary Table 2).

1.36 g_{water} $g_{sorbent}^{-1}$ at 30% RH and 2.36 g_{water} $g_{sorbent}^{-1}$ at 60% RH (Fig. 3b). Moreover, it can achieve ultrahigh water uptake up to 6.61 g_{water} $g_{sorbent}^{-1}$ at 90% RH (Extended Data Fig. 4). The high water uptake at various RHs indicates the climate adaptability of BHNC for all-weather water harvesting from air.

To avoid the solution leakage of BHNC, we propose a facile method to evaluate the maximum water uptake at different RHs (Supplementary Note 2.2). Owing to the high porosity of BPGHM (~97%) (Fig. 2e) and appropriate salt impregnation (~69 wt%) (Supplementary Figs. 14 and 15), the cyclical results show that BHNC has stable multi-step water uptake capacity and can maintain a stable shape with no solution leakage after sorption for 12 h at 90% RH (Extended Data Fig. 5 and Supplementary Fig. 16).

Figure 3c shows the comparison of water uptake between our BHNC and reported state-of-the-art sorbents for SAWH, revealing the BHNC has ultrahigh water uptake under a wide humidity range. At low humidity conditions in an arid region (less than 30% RH), the BHNC shows superior water sorption capacity (1.36 g_{water} $g_{sorbent}^{-1}$ at 30% RH), approximately 2–4 times higher than reported novel physical sorbents[10,39–42]. At high humidity conditions, the BHNC exhibits ultrahigh water uptake (6.61 g_{water} $g_{sorbent}^{-1}$ at 90% RH), much higher than other salt-based composites[16,43,44].

In addition to the superiority of high water uptake, our BHNC also exhibits faster water sorption kinetics than reported salt-based composites[16,18,19,32,45–47] (Fig. 3d and Supplementary Table 2). This is contributed by the bidirectionally aligned hierarchical structures for accelerating water transport.

Water sorption kinetics of scalable BHNC blocks

We further evaluate the water sorption kinetics of scalable BHNC blocks. The water sorption in BHNC block involves multi-step water transport processes (Fig. 4a) and heat/mass transfer resistances (Fig. 4b): surface convective heat/mass transfer at the interface between air and sorbents through vertically oriented millimetre-scale channels, internal heat conduction/mass diffusion within sorbent from the external surface to the intrapore surface through radially oriented micrometre-scale channels and water molecules captured by sorption sites.

We prepared three different nanocomposite blocks with unordered structure, unidirectional structure and bidirectional structure to cross check the accuracy of the abovementioned theoretical analysis (Extended Data Fig. 6, Supplementary Figs. 17 and 18 and Supplementary Table 3). The simulation results are in good agreement with their corresponding experimental results (Supplementary Fig. 19). Both experimental results and theoretical analysis verify the proposed bidirectional structure exhibits the fastest sorption kinetics and the lowest mass transport resistance (Extended Data Fig. 6e and Supplementary Fig. 20). Moreover, our BHNC block shows great potential in scalability because different BHNC blocks can be easily assembled in series and parallel according to the demands of SAWH (Fig. 4c).

To evaluate the possibility of large-scale BHNC assembly, we designed an experimental rig that can control the velocity, temperature and RH of airflow (Supplementary Figs. 21 and 22 and Supplementary Note 2.3). Four BHNC blocks were integrated into one packed unit and then the sorption/desorption kinetics of one to three packed units in series were tested. Either one packed unit or three packed units shows

https://doi.org/10.1038/s44221-023-00150-0

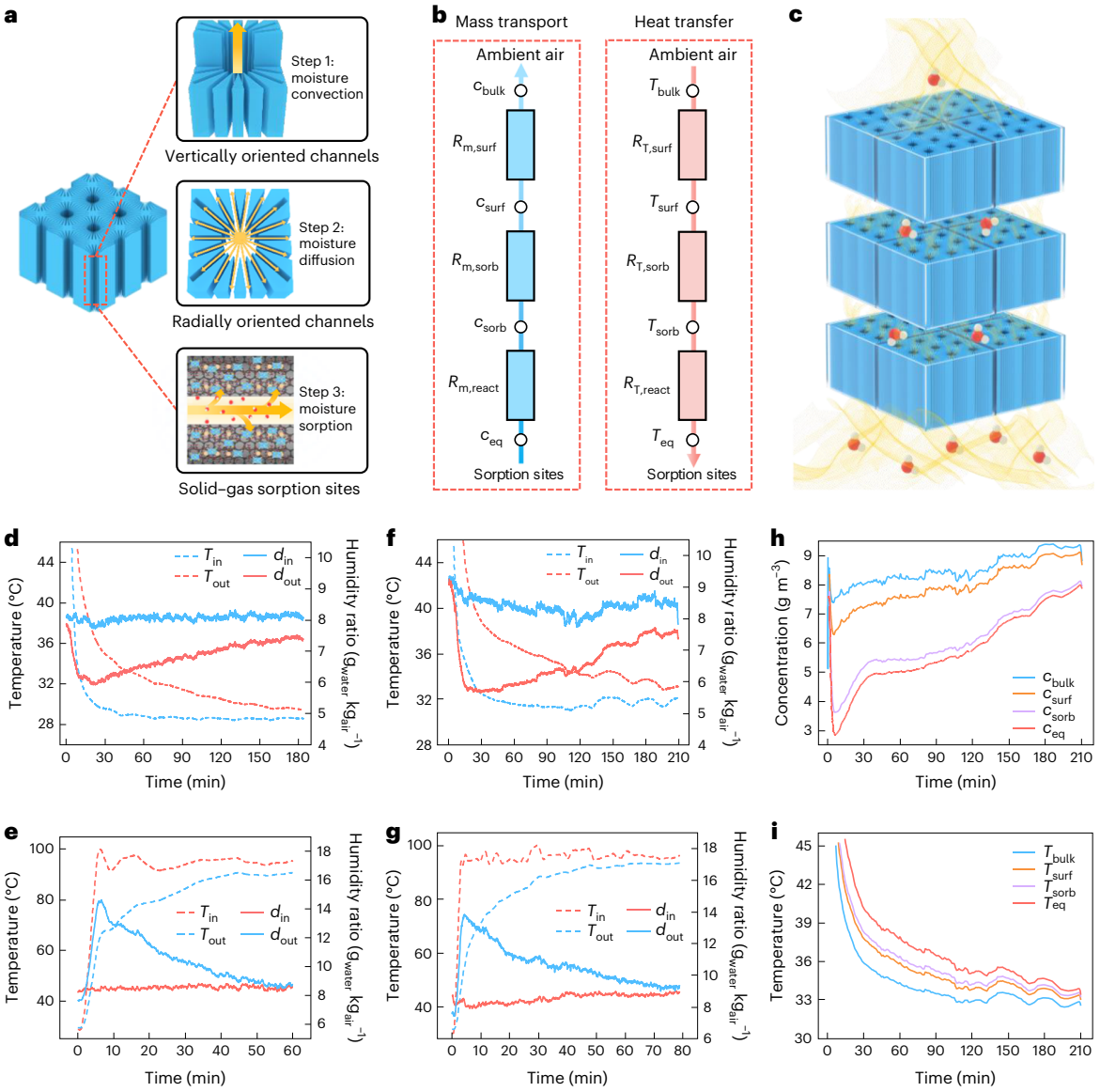

Fig. 4 | Water sorption kinetics of scalable BHNC blocks. a, Diagram of multi-step moisture transport during water sorption process of BHNC, includes moisture convection in vertically oriented millimetre-scale channels, moisture diffusion in radially oriented micrometre-scale channels and moisture sorption at the solid–gas interface. **b**, Corresponding multi-step heat transfer and mass transport networks during the water sorption process: (1) surface heat/mass convective resistance ($R_{T,surf}$ and $R_{m,surf}$) at the interface between air and sorbents; (2) intra heat conduction/mass diffusion resistance ($R_{T,sorb}$ and $R_{m,sorb}$) within sorbent from the extra surface to the intrapore surface; (3) reaction resistance ($R_{T,react}$ and $R_{m,react}$) at sorption sites. **c**, Schematic showing moisture transport in scalable BHNC arrays, where four BHNC blocks are connected in parallel to form a sorbent unit and three sorbent units are connected in series to assemble scalable BHNC arrays as a packed SAWH device. **d**–**g**, Temperature and humidity evolutions of scalable BHNC arrays showing the one sorbent unit (**d**,**e**) and three sorbent units (**f**,**g**). The testing condition for water sorption is under 30 °C 30% RH, and the testing condition for water desorption process is under 90 °C with an airflow rate of around 1.1 m s^{-1}. **h**–**i**, Numerical results show the distribution of average vapour concentration (**h**) and average temperature (**i**) in three sorbent units during water sorption process.

fast water sorption/desorption kinetics (Fig. 4d–g) enabled by the vertically oriented millimetre-scale holes for convection airflow. The sorption and desorption processes of one BHNC packed unit can achieve equilibrium in 180 min and 60 min (Fig. 4d,e). Even with three BHNC packed units assembled in series with the size of 100 × 100 × 120 mm, the sorption and desorption processes can be finished in less than 210 min and 80 min under the same conditions (Fig. 4f,g). Furthermore, the sorption/desorption kinetics can be enhanced by increasing the airflow rate (Supplementary Figs. 23 and 24) and can maintain excellent stability (Supplementary Figs. 25). These results confirm that our BHNC block has great potential for scalable packed sorbents with superior water sorption/desorption kinetics.

We further analysed the influential mechanism of heat-mass transfer resistance by theoretical models with high reliability (Supplementary Note 1 and Supplementary Fig. 26). The large concentration difference mainly occurs between the air-sorbent surface and intra-sorbent ($c_{surf} - c_{intra}$), indicating diffusion resistance has a dominant role during the multi-step mass transport processes (Fig. 4h and Supplementary Fig. 27). Meanwhile, the temperature difference between bulk air and surface ($T_{surf} - T_{bulk}$) dominates the thermal resistance during the heat transfer process (Fig. 4i and Supplementary Fig. 27). Attributing to the synergistic enhancement of heat transfer and mass transport, the sorption heat can be removed timely and moisture can be supplied quickly in the scalable BHNC blocks, thus

accelerating the water sorption/desorption kinetics. It is noted that fast water sorption/desorption rate provides the potential to realize multiple water harvesting cycles.

Demonstration of scalable solar-driven SAWH

We finally engineered a scalable solar-driven SAWH prototype by assembling 24 BHNC blocks in series and parallel arrays (Fig. 5a). This prototype mainly consists of a solar air collector, a heat recovery exchanger, an air-cooled condenser and six BHNC units integrating with 24 BHNC blocks (Fig. 5c and Supplementary Fig. 28). Moreover, the optimized design from material, device and cycle of SAWH system is comprehensively considered for the prototype to realize energy efficient and high-yield water harvesting from air (Supplementary Note 3).

We systematically analysed the energy balance of different SAWH systems by theoretical calculation (Extended Data Fig. 7 and Supplementary Note 4). To realize energy efficient SAWH with high thermal efficiency, we proposed an energy-saving strategy to perform heat recovery between the hot air from nanocomposite to condenser and the warm air from condenser to solar collector (Extended Data Fig. 7c). This energy-saving strategy has synergistic effects of lowering the cooling load of condenser and simultaneously decreasing the heating load of solar collector. Benefiting from the energy-saving design, the thermal efficiency of SAWH system with heat recovery can be improved by two–four times compared with conventional systems (Extended Data Fig. 8), indicating heat recovery is effective in realizing energy efficient atmospheric water harvesting.

Figure 5b shows the psychrometric chart of water capture and collection processes with heat recovery. Heat recovery is carried out to utilize the heat released by hot air (B → C) to preheat warm air (D → E) during the water collection process. The precooled air is further cooled down by ambient air in the condenser to perform water condensation-collection (C → D), while the preheated air is further heated by solar collector (E → A) to drive the BHNC for water desorption (A → B).

The BHNC-based SAWH prototype exhibits rapid-cycling multiple water harvesting cycles during indoor experiments (Extended Data Fig. 9). The heat recovery design improves the thermal efficiency of SAWH (~20.2%) by recovering heat from hot air (Supplementary Table 4), and the total water production within 10 h is as high as 2,820 $ml_{water}\ kg_{sorbent}^{-1}$ (Fig. 5d). The ultrahigh water production is attributed to the multiple water harvesting cycles and high water uptake during every SAWH cycle.

We further performed outdoor experiments using a BHNC-based prototype driven by a solar air collector, realizing rapid-cycling water production and five continuous water capture-collecting cycles during the daytime (Fig. 5e). Hot air temperature reaches 70 ~ 120 °C by the solar collector under irradiation intensity ranging from 400 ~ 1,000 W m^{-2}. The solar-driven SAWH prototype exhibits high water production of up to 2,000 $ml_{water}\ kg_{sorbent}^{-1}\ day^{-1}$ even at very low RH (below 30% RH) (Fig. 5f). Compared with reported SAWH systems, our prototype shows the highest water production during a wide air humidity range (Fig. 5g)[3,16,32,47–51]. Moreover, we found the collected water does not contain lithium element, demonstrating no leakage of LiCl into the water. All elements and ions concentrated in the collected water meet the standard drinking-water quality of World Health Organization (WHO) (Supplementary Tables 5 and 6).

Discussion

We analysed and revealed the essence of the structure–performance relationship of packed sorbents for atmospheric water harvesting. To accelerate water transport and improve sorption/desorption kinetics, we further conceived bidirectional structures for packed sorbents with short diffusion depth and low tortuosity. Inspired by the theoretical analysis, we reported a facile strategy to synthesize bidirectionally aligned and hierarchically structured nanocomposites (BHNC) for scalable and efficient water harvesting from air. The resultant BHNC exhibits ultrahigh water uptake of up to 6.61 $kg_{water}\ kg_{sorbent}^{-1}$ by employing multi-step water sorption processes and ultrafast water sorption/desorption kinetics by introducing vertically oriented moisture convection and radially oriented intrapore diffusion, outperforming the state-of-the-art sorbents.

Our strategy realizes scalable sorbents with ordered hierarchical structures and synergistic enhancement of heat transfer and mass transport for accelerating water sorption/desorption kinetics. We engineered and demonstrated a rapid-cycling solar-driven SAWH prototype by assembling BHNC block arrays with heat recovery. The prototype realizes multiple water capture–collection cycles with high-yield water production of 2,000–2,820 $ml_{water}\ kg_{sorbent}^{-1}\ day^{-1}$. Our strategy of bidirectionally aligned nanocomposites with fast sorption kinetics, rapid-cycling scalable SAWH devices with enhanced heat transfer and mass transport and energy efficient SAWH systems with heat recovery cycle provides new insights into the development of next-generation materials, devices and systems for atmospheric water harvesting.

Methods

Chemicals and materials

Natural flake graphite (325 mesh, 99.9 wt%) was purchased from XFNANO Co. Sodium nitrate ($NaNO_3$, 99.5 wt%), potassium permanganate ($KMnO_4$, 99.5 wt%), sulfuric acid (H_2SO_4, >96.0%), hydrochloric acid (HCl, 36.0 ~ 38.0%) and hydrogen peroxide (H_2O_2) were purchased from Sinopharm Chemical Reagent Co. Sodium alginate, calcium chloride ($CaCl_2$, 96.0%) and lithium chloride (LiCl, 99%) were purchased from MERYER Shanghai Chemical Technology Co.

Synthesis of bidirectionally aligned and hierarchically structured nanocomposites

The graphene oxide (GO) was prepared by the modified Hummer method. In a typical synthesis procedure, 50.0 g GO aqueous suspension (10 mg ml^{-1}) was first prepared by ultrasonication (100 W for 30 min). 4.0 g SA solution was added to 96.0 g deionized water, then magnetically stirred at 80 °C until completely dissolved. Afterward, 50.0 g GO aqueous suspension, 50.0 g deionized water and 100.0 g SA solution were mixed and magnetically stirred until uniformly mixed. The as-prepared GO-SA suspension was poured into the specially designed mould with a dimension of 50 × 50 × 50 mm. The mould is composed of a copper base with arrayed copper pillars and a Teflon wall. After freezing with liquid nitrogen and drying in a vacuum freeze dryer (<1 Pa) for three days, the GO-SA framework with a bidirectionally aligned porous structure is obtained. Then the framework was immersed in $CaCl_2$ solution (2 wt%) for 24 hours to let the Ca^{2+} partially replace the Na^+ to make the alginate form cross-linked networks to enhance the mechanical strength. After freeze drying, the bidirectionally aligned and cross-linked GO-SA framework was subsequently treated at 120 °C to become a bidirectionally aligned porous graphene hydrogel matrix (BPGHM) with ordered hierarchical structures. Finally, the BPGHM was immersed in LiCl solution (10 wt%) and dried to gain bidirectionally aligned and hierarchically structured nanocomposites (BHNC). An infrared camera (FLIR T630sc) was employed to measure the temperature distribution when pouring the solution into the bidirectional freeze-casting moulds.

In addition, the unordered-aligned nanocomposites and unidirectional-aligned nanocomposites used for cross checking the accuracy of theoretical analysis were prepared based on the same chemicals and preparation methods. The differences between the three structures are the moulds and freezing way. For unordered-aligned nanocomposites, the mould is a Teflon base and enclosure wall with low thermal conductivity. The mould for unidirectional structural nanocomposites is a Teflon base with acrylic pillars (with similar low thermal conductivity with Teflon) enclosed by a Teflon wall. A non-directional freezing way was conducted for these two structured nanocomposites.

https://doi.org/10.1038/s44221-023-00150-0

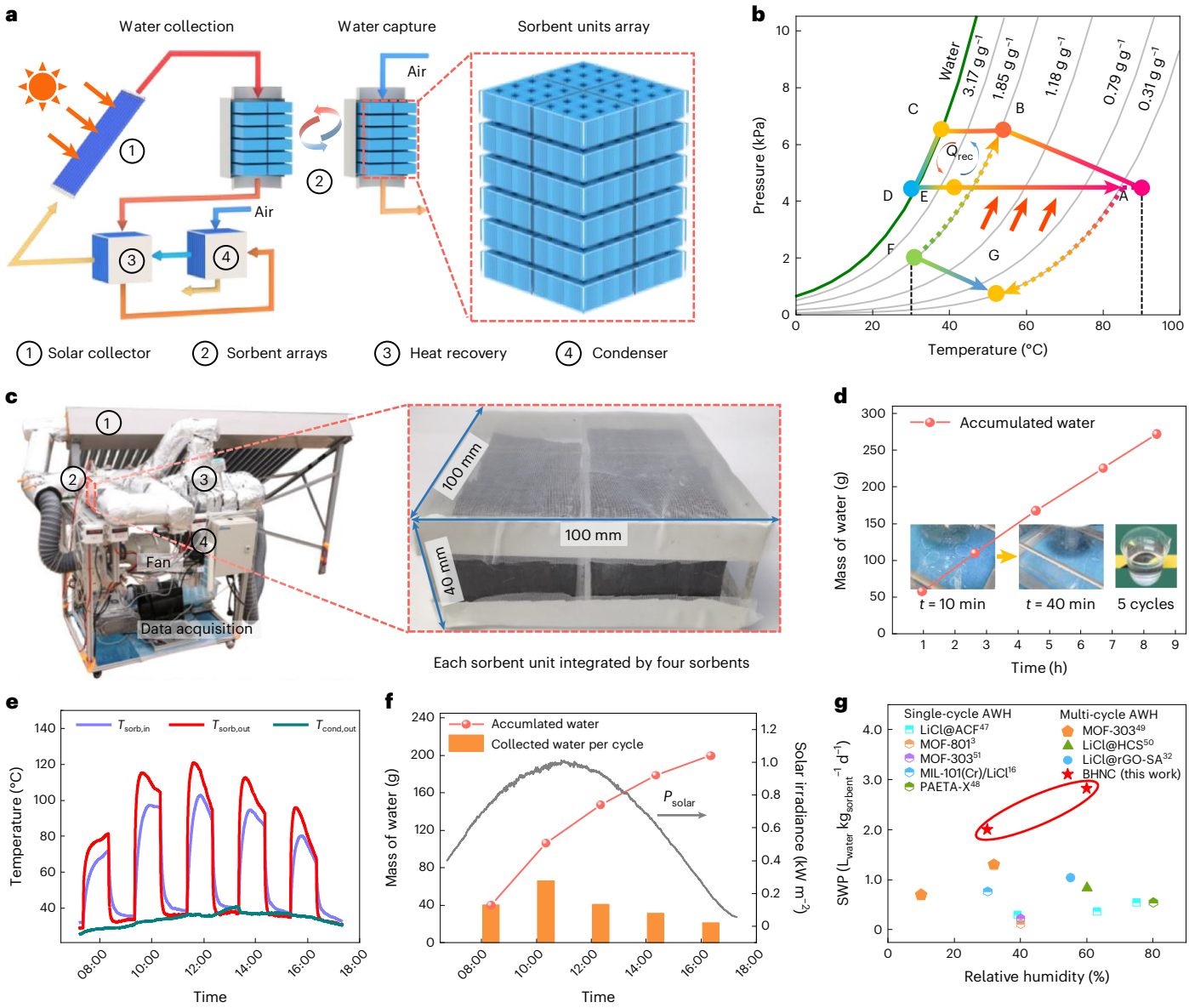

Fig. 5 | Demonstration of scalable and efficient solar-driven SAWH prototype with BHNC arrays. a, Operating principles of solar-driven SAWH prototype with heat recovery cycle for energy efficient and rapid-cycling water harvesting from air. **b**, Psychrometric chart showing water capture process (F → G) and water collection process (A → B → C → D → E → A) of SAWH. During water capture, the BHNC captures moisture from ambient air in open mode. The air becomes warm and dry after water sorption and finally discharges into the ambient. During water collection, the BHNC performs water desorption by releasing captured water to the condenser in closed mode. Heat recovery between high-temperature air to the condenser (B → C) and low-temperature air to the solar collector (D → E) improves thermal efficiency. Q_{rec} is the amount of energy by heat recovery. **c**, Digital photograph of one sorbent unit formed by four BHNC blocks and scalable solar-driven SAWH prototype assembled by six sorbent units (24 BHNC blocks in total). **d**, Water harvesting capacity per cycle and accumulated collected water under 60% RH during indoor experiments. The insets show digital photographs of collected water at different times. **e**, Demonstration of solar-driven SAWH device for multiple water harvesting cycles during outdoor experiments. **f**, Water harvesting capacity under 30% RH at 30 °C during outdoor experiments in Shanghai, China. **g**, Comparison of water production at different RH conditions between our SAWH device and reported water harvesters[3,16,32,47,51].

Characterization of BHNC

The morphologies and structures of GO-SA, BPGHM and BHNC were characterized by a field emission scanning electron microscope (Sirion 200 instrument, FEI) equipped with energy disperse X-ray spectroscopy (INCA X-Act attachment, Oxford). The GO, GO-SA and BPGHM were characterized by X-ray photoelectron spectroscopy (AXIS Ultra DLD) using a monochromatic Al-Ka X-ray source. The pore size distributions of BPGHM and BHNC were measured by an automatic mercury porosimeter (Micromeritics AutoPore Iv 9510). The X-ray diffraction patterns of GO, GO-SA, BPGHM and BHNC were measured by a polyfunctional X-ray diffractometer (D8 ADVANCE Da Vinci, Bruker) at different temperatures. The contact angles between the samples (compressed into tablet under 5 MPa) and water droplet were measured by using a contact angle instrument (DSA100, Kruss).

Water sorption of BHNC

The water sorption isotherms of BHNC at different humidity conditions were measured by an adsorption apparatus (ASAP 2020 plus, Micromeritics) under different temperatures. The water sorption/desorption tests were performed on a thermogravimetric analyser (STA 449 C, Netzsch), equipped with a moisture humidity generator (MHG 32, ProUmid). First, the BHNC sample was completely dried at 90 °C.

Then, the sample was placed inside a thermogravimetric analyser and kept at 30 °C for a given humidity condition (15%, 30%, 60%) for 8 hours for sorption. After that, the sample was heated at 90 °C with a vapour pressure of 4.2 kPa for 4 hours to regenerate BHNC.

The water uptake capacity of BHNC materials was tested using a constant temperature and humidity chamber (KMF-115, Binder) for sorption (30 °C, 90% RH) after fully desorbed in an oven (BGZ-30, BOXUN) and electronic balance with an accuracy of 0.1 mg (ME204, METTLER TOLEDO) was used for the mass measurement.

The cyclical stability of milligram-level BHNC materials under low RH (30%) and high RH (80%) was tested on a thermogravimetric analyser (STA 449 C, Netzsch), equipped with a moisture humidity generator (MHG 32, ProUmid) by switching between 30 °C with 30% RH (or 80% RH) and 90 °C with a vapour pressure of 4.2 kPa for multiple heating/cooling cycles.

The comparison of sorption kinetics for different nanocomposites mentioned in the morphological evolution was conducted in our designed device, where the airflow rate was adjusted with an electric fan and a.c./d.c. adaptor. A wind velocity sensor (WD400, 0–2 m s^{-1} with accuracy of 3%) and two temperature and humidity sensors (MIK-TH800, operating at −40 to 120 °C with a temperature accuracy of ±0.3 °C and humidity accuracy of ±2% RH) were installed. The real-time signals from these sensors were collected using a data collector (34970 A, Agilent) and recorded on a computer. An electronic balance with an accuracy of 1 mg (503TE, METTLER TOLEDO) was used for the mass measurement, and the real-time mass data were collected and recorded on a computer. The cyclical stability of the sorption/desorption kinetics of the BHNC block was also tested using our designed device under a controlled environmental condition (30 °C, 30% RH for sorption and 90 °C for desorption). Four electric heaters and a temperature control module were added to heat the air for the desorption process.

Performance of BHNC-based SAWH system

The SAWH device is assembled by a metal enclosure with a dimension of 100 × 100 × 200 mm and BHNC arrays with a dimension of 100 × 100 × 40 mm. Four BHNC blocks with a pore size of 3 mm, an interval of 6 mm and a length of 40 mm are used to assemble a sorption unit. The bulk density of the sorption unit is 0.12 g cm^{-3}. Temperature sensors (PT100, with an accuracy of ±0.15 °C) and humidity sensors (MIK-TH800, operating at −40 to 120 °C with a temperature accuracy of ±0.3 °C and humidity accuracy of ±2% RH) are installed at the inlet and outlet channels of SAWH device. The heat recovery and condenser are composed of air-to-air heat exchangers with dimensions of 200 × 200 × 200 mm. The heat exchanger is fabricated by hydrophilic aluminium with an interval of 3.5 mm. The air-to-air heat exchanger is used for two cross-flow air without mass exchange. For heat recovery, the hot humidity air (typically 50–90 °C with an airflow rate of 50–90 m^3 h^{-1}) from the outlet of the SAWH device is driven by an electric fan (HG-HF-100P, 90 W with a maximum airflow rate of 366 m^3 h^{-1} and maximum air pressure of 578 Pa) to first flow through the SAWH device and then to the heat recovery–condenser and the solar heater, then back to the SAWH device. An electric heater fabricated by a PTC heater and aluminium fins with a maximum heating power of 2,400 W is used to simulate an external heat source for driving water desorption during indoor experiments. The amount of electricity consumption is recorded by an electricity meter. A solar air collector is fabricated by 20 evacuated solar collector tubes with a diameter of 58 mm and a length of 1.8 m. The air from the outlet of heat recovery or condenser will flow into the solar thermal collector, which can be heated to 80–120 °C with solar-to-heat efficiency of around 46–55%. The outlet hot air will directly flow into the SAWH device to drive the desorption process of nanocomposite. The concentrations of possible elements and ions in collected water were measured by inductively coupled plasma analysis (Avio 500, Perkin-Elmer) and ion chromatography (ICS-5000 + /900, Thermofisher).

Data availability

All relevant data that support the results of this study are presented in the main text and Supplementary Information. Source data are provided as an Excel file with the Supplementary Information. Source data are provided with this paper.

References

1. Mekonnen, M. M. & Hoekstra, A. Y. Four billion people facing severe water scarcity. *Sci. Adv.* **2**, e1500323 (2016).
2. Lord, J. et al. Global potential for harvesting drinking water from air using solar energy. *Nature* **598**, 611–617 (2021).
3. Kim, H. et al. Water harvesting from air with metal-organic frameworks powered by natural sunlight. *Science* **356**, 430–434 (2017).
4. Wang, Y., Zhao, W., Han, M., Xu, J. & Tam, K. C. Biomimetic surface engineering for sustainable water harvesting systems. *Nat. Water* **1**, 587–601 (2023).
5. Tu, Y., Wang, R., Zhang, Y. & Wang, J. Progress and expectation of atmospheric water harvesting. *Joule* **2**, 1452–1475 (2018).
6. Hanikel, N., Prévot, M. S. & Yaghi, O. M. MOF water harvesters. *Nat. Nanotechnol.* **15**, 348–355 (2020).
7. Ejeian, M. & Wang, R. Adsorption-based atmospheric water harvesting. *Joule* **5**, 1678–1703 (2021).
8. Lin, H., et al. Metal–organic frameworks for water harvesting and concurrent carbon capture: a review for hygroscopic materials. *Adv. Mater*. https://doi.org/10.1002/adma.202209073 (2023).
9. Kalmutzki, M. J., Diercks, C. S. & Yaghi, O. M. Metal–organic frameworks for water harvesting from air. *Adv. Mater.* **30**, e1704304 (2018).
10. Hanikel, N. et al. Evolution of water structures in metal-organic frameworks for improved atmospheric water harvesting. *Science* **374**, 454–459 (2021).
11. Rieth, A. J. et al. Record-setting sorbents for reversible water uptake by systematic anion exchanges in metal–organic frameworks. *J. Am. Chem. Soc.* **141**, 13858–13866 (2019).
12. Nguyen, H. L. Covalent organic frameworks for atmospheric water harvesting. *Adv. Mater.* **35**, 2300018 (2023).
13. Sun, C., Sheng, D., Wang, B. & Feng, X. Covalent organic frameworks for extracting water from air. *Angew. Chem. Int. Ed.* **135**, e202303378 (2023).
14. Nguyen, H. L. et al. Hydrazine-hydrazide-linked covalent organic frameworks for water harvesting. *ACS Cent. Sci.* **8**, 926–932 (2022).
15. Sun, C. et al. 2D covalent organic framework for water harvesting with fast kinetics and low regeneration temperature. *Angew. Chem. Int. Ed.* **62**, e202217103 (2023).
16. Xu, J. et al. Efficient solar-driven water harvesting from arid air with metal–organic frameworks modified by hygroscopic salt. *Angew. Chem. Int. Ed.* **59**, 5202–5210 (2020).
17. Lu, H. et al. Tailoring the desorption behavior of hygroscopic gels for atmospheric water harvesting in arid climates. *Adv. Mater.* **34**, 2205344 (2022).
18. Li, R., Shi, Y., Wu, M., Hong, S. & Wang, P. Improving atmospheric water production yield: enabling multiple water harvesting cycles with nano sorbent. *Nano Energy* **67**, 104255 (2020).
19. Entezari, A., Ejeian, M. & Wang, R. Super atmospheric water harvesting hydrogel with alginate chains modified with binary salts. *ACS Mater. Lett.* **2**, 471–477 (2020).
20. Yan, T. et al. Ultrahigh-energy-density sorption thermal battery enabled by graphene aerogel-based composite sorbents for thermal energy harvesting from air. *ACS Energy Lett.* **6**, 1795–1802 (2021).
21. Garzón-Tovar, L., Pérez-Carvajal, J., Imaz, I. & Maspoch, D. Composite salt in porous metal-organic frameworks for adsorption heat transformation. *Adv. Funct. Mater.* **27**, 1606424 (2017).

22. Shan, H. et al. Exceptional water production yield enabled by batch-processed portable water harvester in semi-arid climate. *Nat. Commun.* **13**, 5406 (2022).
23. Chen, Z. et al. Study of the scale-up effect on the water sorption performance of MOF materials. *ACS Mater. Au* **3**, 43–54 (2022).
24. Li, R. & Wang, P. Sorbents, processes and applications beyond water production in sorption-based atmospheric water harvesting. *Nat. Water* **1**, 573–586 (2023).
25. Song, Y. et al. High-yield solar-driven atmospheric water harvesting of metal–organic-framework-derived nanoporous carbon with fast-diffusion water channels. *Nat. Nanotechnol.* **17**, 857–863 (2022).
26. Gordeeva, L. G. et al. Metal–organic frameworks for energy conversion and water harvesting: a bridge between thermal engineering and material science. *Nano Energy* **84**, 105946 (2021).
27. Hua, L., Xu, J. & Wang, R. Exergy-efficient boundary and design guidelines for atmospheric water harvesters with nano-porous sorbents. *Nano Energy* **85**, 105977 (2021).
28. Song, W., Zheng, Z., Alawadhi, A. H. & Yaghi, O. M. MOF water harvester produces water from Death Valley desert air in ambient sunlight. *Nat. Water* **1**, 626–634 (2023).
29. Ruthven, D. M., Kärger, J. & Theodorou, D. N. *Diffusion in Nanoporous Materials* (John Wiley & Sons, 2012).
30. LaPotin, A., Kim, H., Rao, S. R. & Wang, E. N. Adsorption-based atmospheric water harvesting: impact of material and component properties on system-level performance. *Acc. Chem. Res.* **52**, 1588–1597 (2019).
31. Díaz-Marín, C. D. et al. Kinetics of sorption in hygroscopic hydrogels. *Nano Lett.* **22**, 1100–1107 (2022).
32. Xu, J. et al. Ultrahigh solar-driven atmospheric water production enabled by scalable rapid-cycling water harvester with vertically aligned nanocomposite sorbent. *Energy Environ. Sci.* **14**, 5979 (2021).
33. Wang, J. et al. High-yield and scalable water harvesting of honeycomb hygroscopic polymer driven by natural sunlight. *Cell Rep. Phys. Sci.* **3**, 100954 (2022).
34. Shao, G., Hanaor, D. A., Shen, X. & Gurlo, A. Freeze casting: from low-dimensional building blocks to aligned porous structures—a review of novel materials, methods, and applications. *Adv. Mater.* **32**, 1907176 (2020).
35. Qiu, L., Liu, J. Z., Chang, S. L., Wu, Y. & Li, D. Biomimetic superelastic graphene-based cellular monoliths. *Nat. Commun.* **3**, 1241 (2012).
36. Hu, X. et al. Tailoring graphene oxide-based aerogels for efficient solar steam generation under one sun. *Adv. Mater.* **29**, 1604031 (2017).
37. Wang, C. et al. Freeze-casting produces a graphene oxide aerogel with a radial and centrosymmetric structure. *ACS Nano* **12**, 5816–5825 (2018).
38. Bai, H., Chen, Y., Delattre, B., Tomsia, A. P. & Ritchie, R. O. Bioinspired large-scale aligned porous materials assembled with dual temperature gradients. *Sci. Adv.* **1**, e1500849 (2015).
39. Furukawa, H. et al. Water adsorption in porous metal-organic frameworks and related materials. *J. Am. Chem. Soc.* **136**, 4369–4381 (2014).
40. Rieth, A. J., Yang, S., Wang, E. N. & Dincă, M. Record atmospheric fresh water capture and heat transfer with a material operating at the water uptake reversibility limit. *ACS Cent. Sci.* **3**, 668–672 (2017).
41. Liu, Z. et al. Ultralow-temperature-driven water-based sorption refrigeration enabled by low-cost zeolite-like porous aluminophosphate. *Nat. Commun.* **13**, 193 (2022).
42. Nguyen, H. L. et al. A porous covalent organic framework with voided square grid topology for atmospheric water harvesting. *J. Am. Chem. Soc.* **142**, 2218–2221 (2020).
43. Guan, W., Lei, C., Guo, Y., Shi, W. & Yu, G. Hygroscopic-microgels-enabled rapid water extraction from arid air. *Adv. Mater.* **35**, e2300296 (2023).
44. Yao, H. et al. Highly efficient clean water production from contaminated air with a wide humidity range. *Adv. Mater.* **32**, 1905875 (2020).
45. Li, R. et al. Hybrid hydrogel with high water vapor harvesting capacity for deployable solar-driven atmospheric water generator. *Environ. Sci. Technol.* **52**, 11367–11377 (2018).
46. Kallenberger, P. A. & Fröba, M. Water harvesting from air with a hygroscopic salt in a hydrogel–derived matrix. *Commun. Chem.* **1**, 28 (2018).
47. Wang, J., Wang, R., Tu, Y. & Wang, L. Universal scalable sorption-based atmosphere water harvesting. *Energy* **165**, 387–395 (2018).
48. Wu, M. et al. Metal- and halide-free, solid-state polymeric water vapor sorbents for efficient water-sorption-driven cooling and atmospheric water harvesting. *Mater. Horiz.* **8**, 1518–1527 (2021).
49. Hanikel, N. et al. Rapid cycling and exceptional yield in a metal-organic framework water harvester. *ACS Cent. Sci.* **5**, 1699–1706 (2019).
50. Yang, K. et al. Hollow spherical SiO_2 micro-container encapsulation of LiCl for high-performance simultaneous heat reallocation and seawater desalination. *J. Mater. Chem. A* **8**, 1887–1895 (2020).
51. Kim, H. et al. Adsorption-based atmospheric water harvesting device for arid climates. *Nat. Commun.* **9**, 1191 (2018).

Acknowledgements

This work was supported by the National Natural Science Funds for Distinguished Young Scholar of China (number 52325601) and the Major Program of National Natural Science Foundation of China (number 52293412). G.Y. acknowledges the support from Camille–Dreyfus Teacher–Scholar Award and the Welch Foundation Award F-1861.

Author contributions

T.L. conceived and designed the experiments. T.Y. and P.W. designed, synthesized and characterized nanocomposites. T.Y. carried out the water sorption–desorption kinetics simulation. T.Y. and P.W. engineered and tested the atmospheric water harvester. P.W. carried out extended experiments according to the comments from reviewers. T.L., T.Y. and P. W. wrote and edited the manuscript. J.X., X.H., Z.B. and W. S. discussed the results and revised the manuscript. G.Y. and R.W. commented on the manuscript. T.L., G.Y. and R.W. supervised the project.

Competing interests

The authors declare no competing interests.

Additional information

Extended data is available for this paper at https://doi.org/10.1038/s44221-023-00150-0.

Supplementary information The online version contains supplementary material available at https://doi.org/10.1038/s44221-023-00150-0.

Correspondence and requests for materials should be addressed to Tingxian Li, Guihua Yu or Ruzhu Wang.

Peer review information *Nature Water* thanks Renyuan Li, Yu Han and the other, anonymous, reviewer(s) for their contribution to the peer review of this work.

https://doi.org/10.1038/s44221-023-00150-0

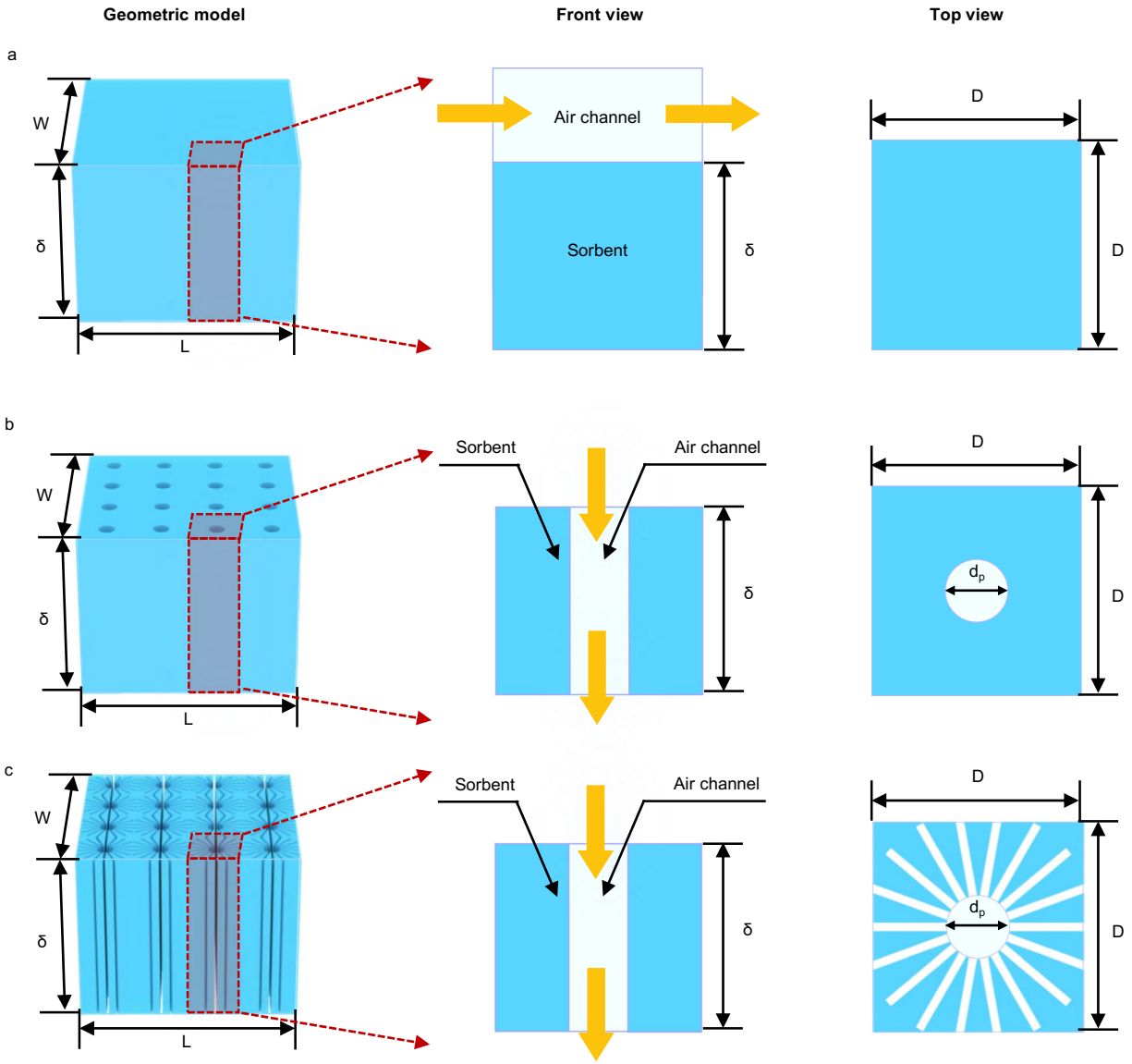

Extended Data Fig. 1 | Numerical models of three nanocomposites with different packed structures. a, Unordered structure. **b**, Unidirectional structure. **c**, Bidirectional structure.

https://doi.org/10.1038/s44221-023-00150-0

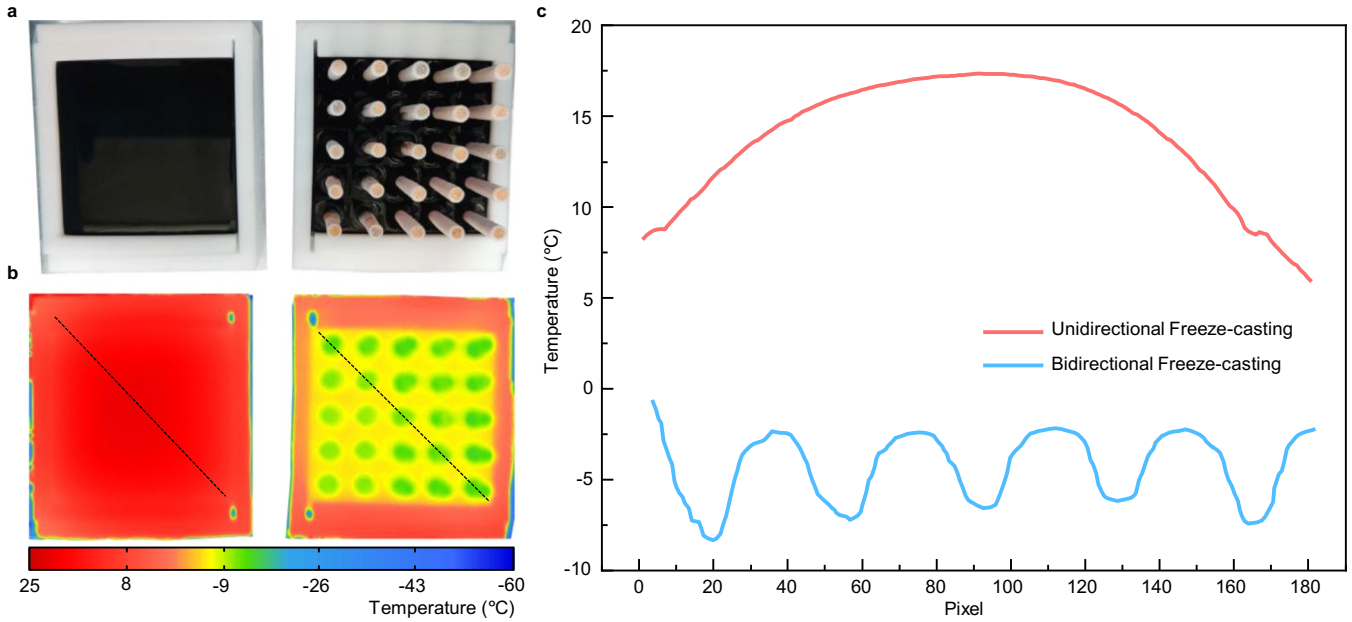

Extended Data Fig. 2 | Temperature distributions of conventional unidirectional freeze-casting method and bidirectional freeze-casting method. a, Digital photograph of two templates for unidirectional freeze-casting method (left) and the proposed bidirectional freeze-casting method (right). **b**, Infrared images showing the temperature distributions of unidirectional freeze-casting method (left) and the proposed bidirectional freeze-casting method (right). **c**, Temperature data of two freeze-casting methods obtained from an infrared temperature map along the dashed line, verifying an additional radial temperature gradient of the proposed bidirectional freeze-casting method.

https://doi.org/10.1038/s44221-023-00150-0

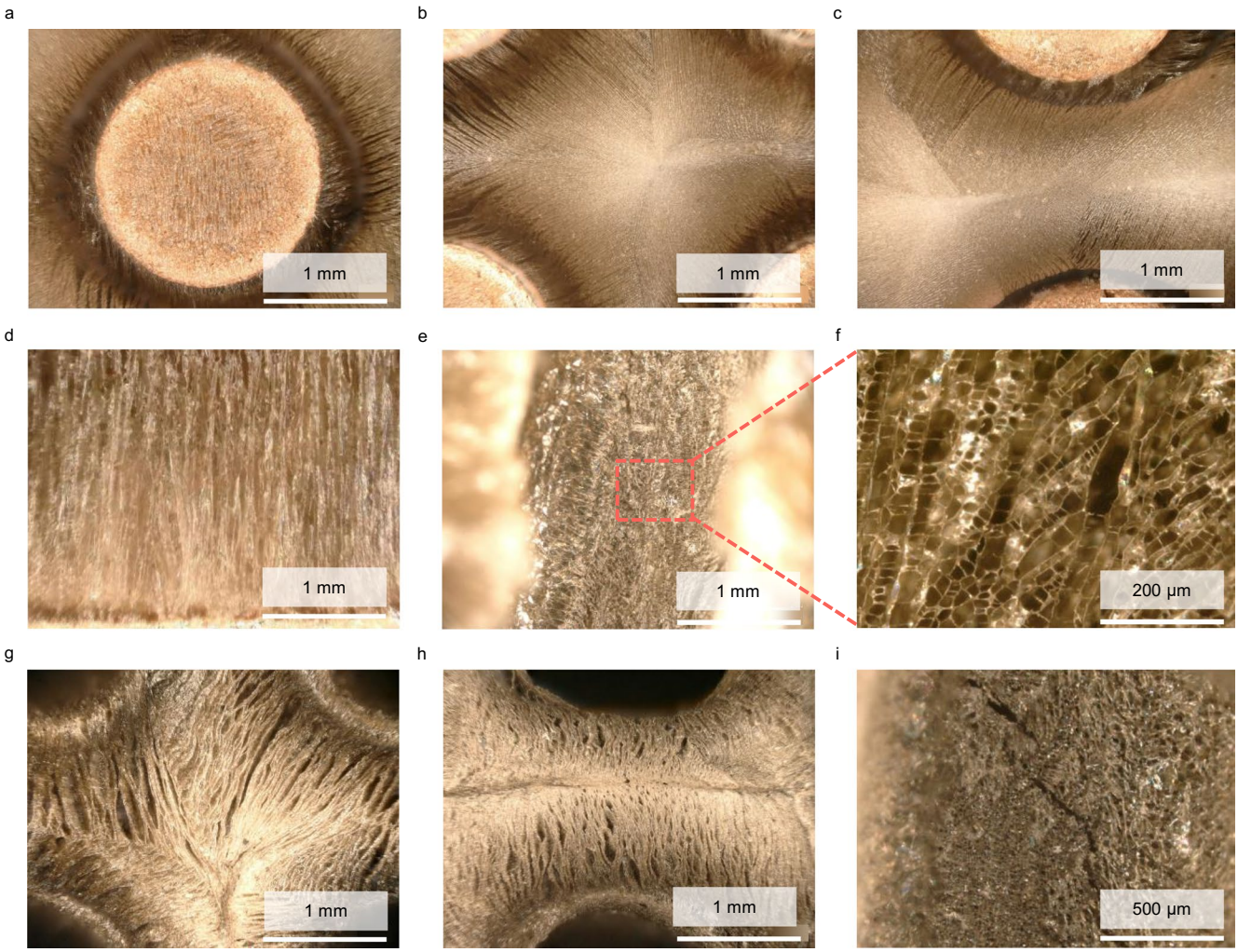

Extended Data Fig. 3 | Images of BHGHM by optical microscope. a–c, Top views of the corner between the arrayed millimeter-sized pores. **d**, Sectional view of the outer wall of BPGHM. **e, f**, Sectional views of the inner wall of BPGHM. **g, h**, Top views of the crosslinked BPGHM. **i**, Sectional view of the inner wall of crosslinked BPGHM.

https://doi.org/10.1038/s44221-023-00150-0

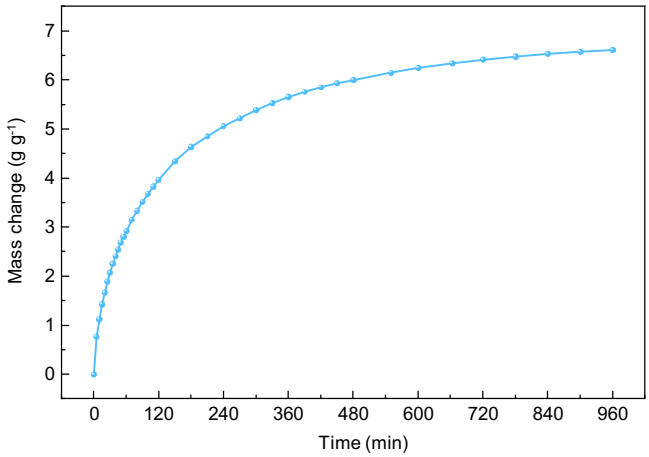

Extended Data Fig. 4 | Water uptake capacity of BHNC under high RH (30 °C, 90%RH). The BHNC block shows superior water uptake capacity of up to 6.61 g g^{-1}.

https://doi.org/10.1038/s44221-023-00150-0

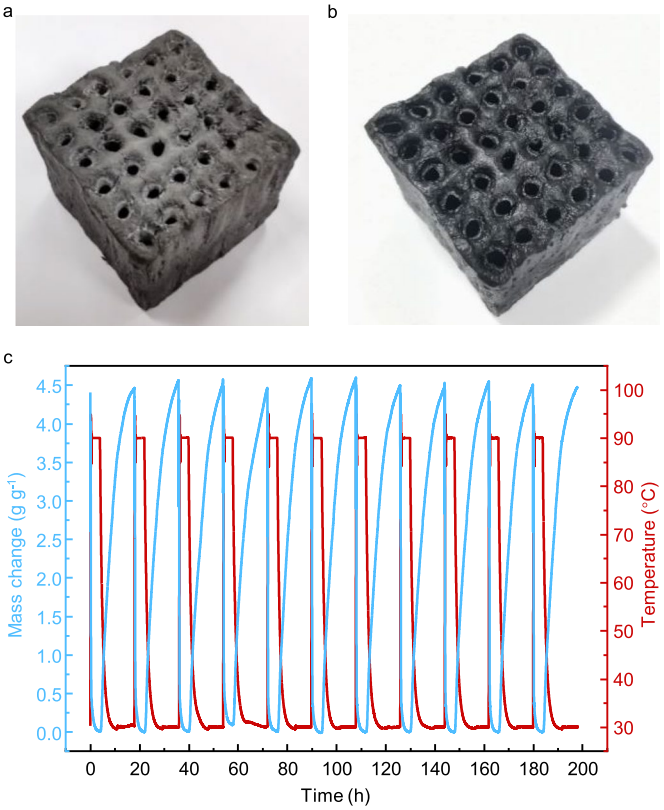

Extended Data Fig. 5 | Cyclical stability tests of BHNC block under high RH. a, b, Digital photographs of BHNC block before (a) and after (b) water sorption at 30 °C and 90% RH for 12 h. **c**, Cyclical tests of milligram-level BHNC by thermogravimetric analyzer during repeated sorption-desorption cycles under 80% RH (30 °C, 80% RH for sorption and 90 °C, 4200 Pa for desorption.

https://doi.org/10.1038/s44221-023-00150-0

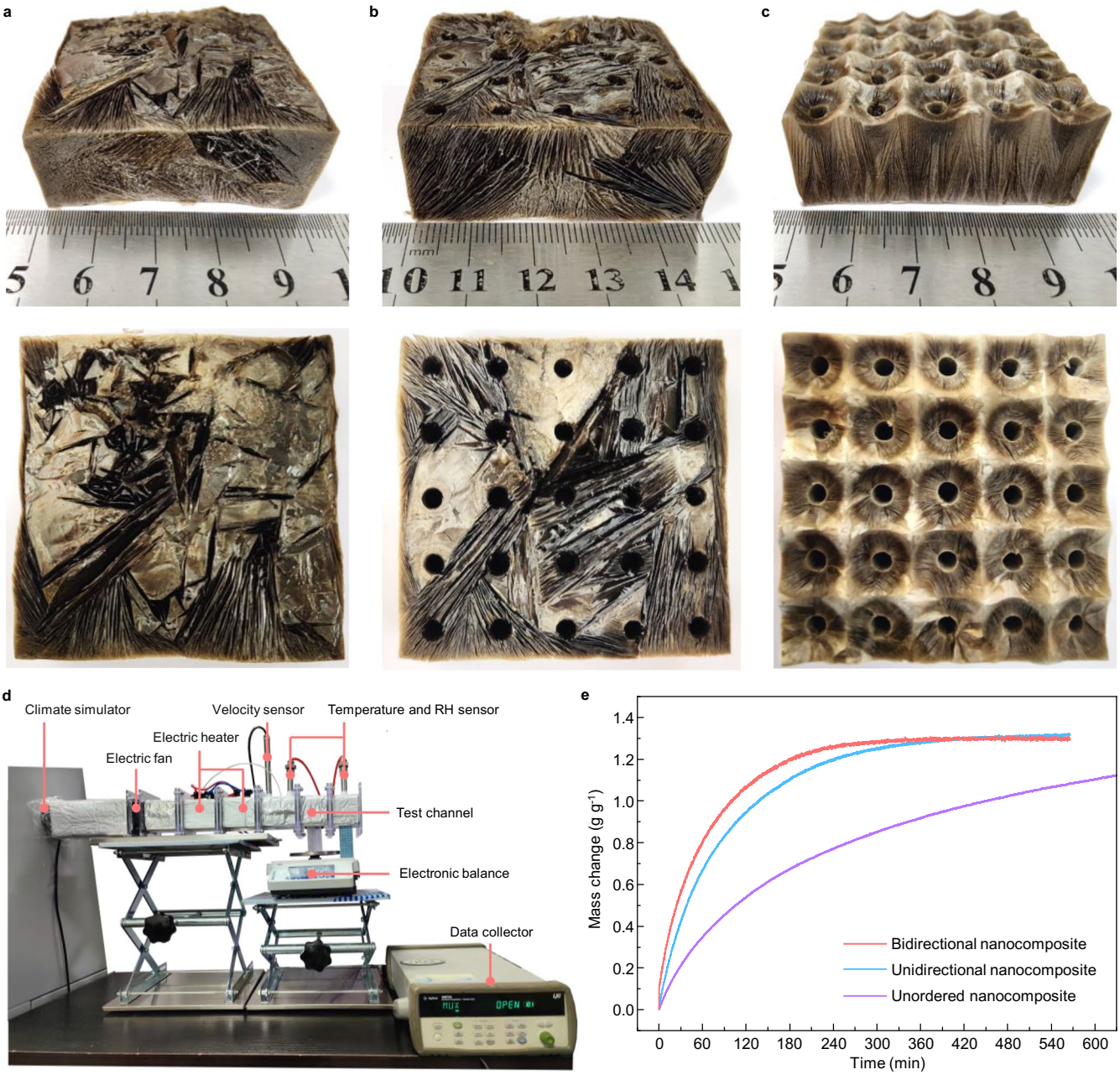

Extended Data Fig. 6 | Digital photographs and sorption kinetics tests of different nanocomposites with unordered, unidirectional, and bidirectional structures. a–c, Digital photographs of different nanocomposites with unordered (a), unidirectional (b), and bidirectional (c) structure (same size of 45 mm × 45 mm × 15 mm). **d**, Digital photograph of experimental device for testing the sorption kinetics of different nanocomposites with unordered, unidirectional, and bidirectional structures. **e**, Experimental results of the sorption kinetics obtained from different nanocomposites with unordered, unidirectional, and bidirectional structures.

https://doi.org/10.1038/s44221-023-00150-0

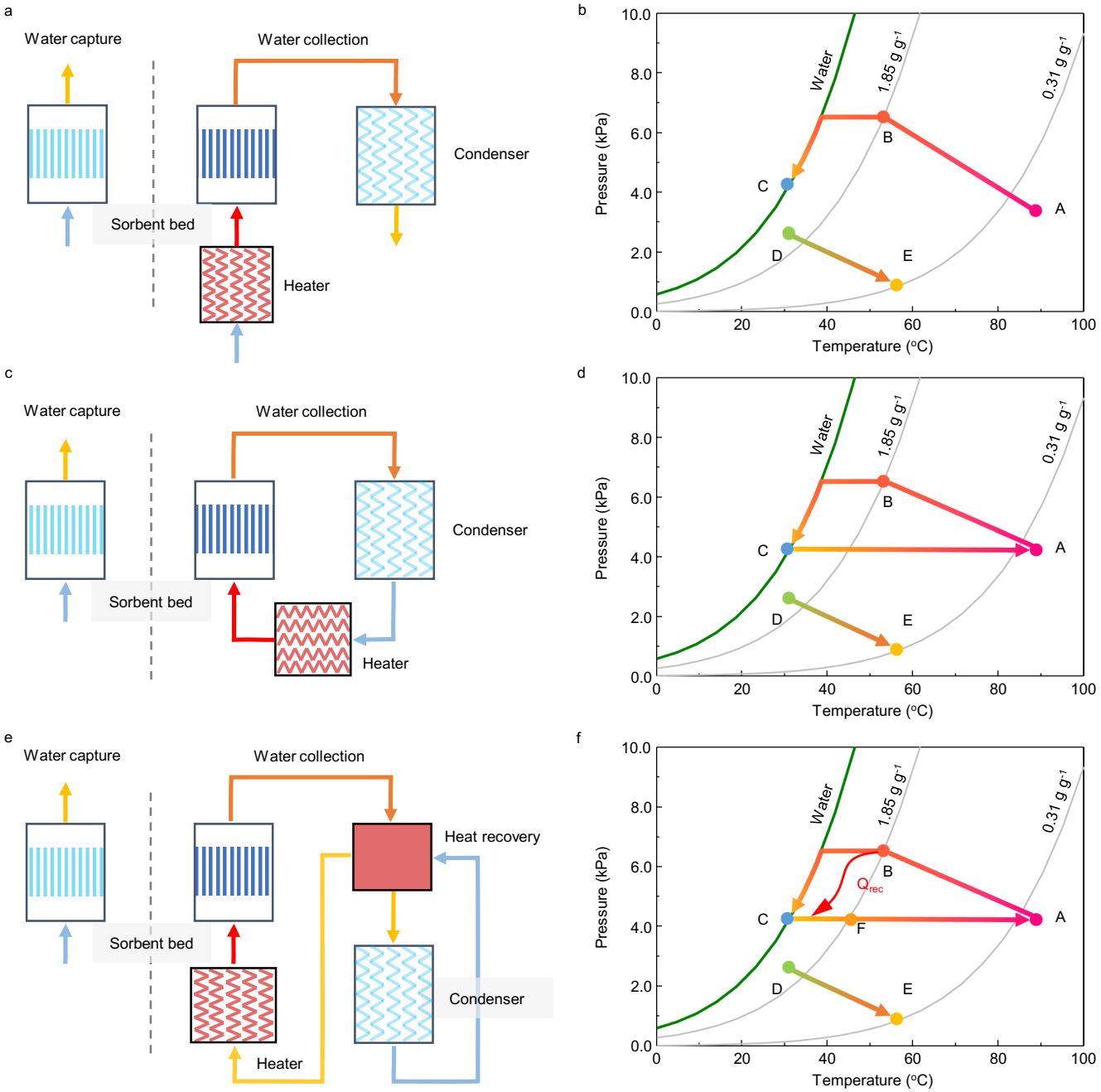

Extended Data Fig. 7 | Schematic diagram and psychrometric charts of different water harvesting systems. a, b, Open air-forced water harvesting system, showing low water-collecting and thermal efficiency due to the inevitable losses of moisture and heat to the ambient. Capture cycle: D → E. Collecting cycle: A → B → C. **c, d**, Close air-forced water harvesting system, still suffering from low thermal efficiency. Capture cycle: D → E. Collecting cycle: A → B → C → A. **e, f**, Closed air-forced water harvesting system with heat recovery cycle, exhibiting superior energy-saving capacity. Capture cycle: D → E. Collecting cycle: A → B → C → A.

https://doi.org/10.1038/s44221-023-00150-0

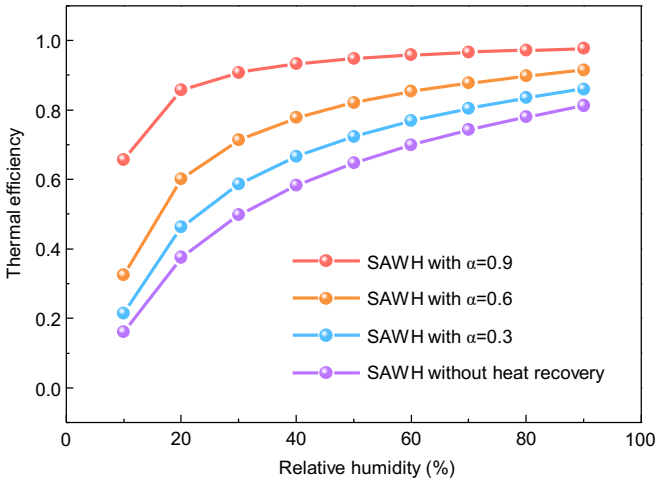

Extended Data Fig. 8 | Thermal efficiency of SAWH with heat recovery under different RH conditions. Thermal efficiency of SAWH increases with increasing heat recovery ratio (α), indicating heat recovery is effective to improve the energy efficiency of SAWH.

https://doi.org/10.1038/s44221-023-00150-0

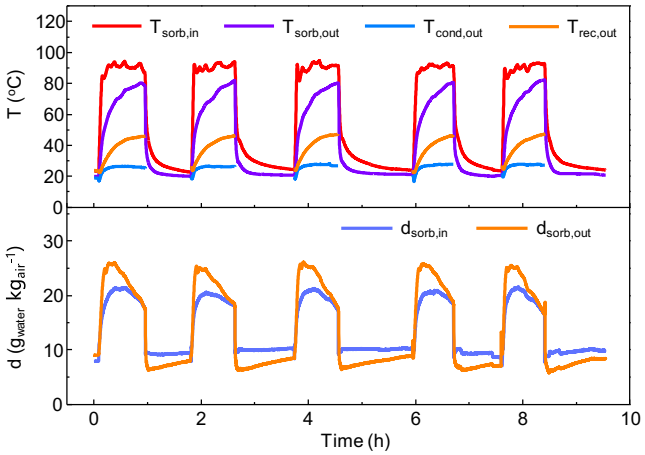

Extended Data Fig. 9 | Temperature and humidity evolutions of BHNC-based SAWH device during the indoor experiments (under 60% RH at 20 °C). The experimental results show our BHNC-based SAWH prototype has rapid-cycling multiple water harvesting cycles during indoor experiments. The temperature of BHNC arrays rapidly increases from ambient temperature (23 °C) to desorption temperature (85 °C) during the water collection stage, and air humidity increases along with water desorption. During the water capture stage, the BHNC arrays capture moisture from ambient air, and the air humidity decreases along with water sorption. The BHNC-based SAWH prototype realizes five water harvesting cycles in 10 h.